Theoretical description of pseudocubic manganites

Chungwei Lin and Andrew J. Millis
Department of Physics, Columbia University, 538W 120th Street, New York, New York 10027, USA
(Received 5 August 2008; published 18 November 2008)

A comprehensive theoretical model for the bulk manganite system $La_{1-x}(Ca,Sr)_xMnO_3$ is presented. The model includes local and cooperative Jahn-Teller distortions and the on-site Coulomb and exchange interactions. The model is solved in the single-site dynamical mean-field approximation using a solver based on the semiclassical approximation. The model semiquantitatively reproduces the observed phase diagram for the doping $0 \leq x < 0.5$ and implies that the manganites are in the strong-coupling region but close to Mott insulator/metal phase boundary. The results establish a formalism for use in a broader range of calculations, for example, on heterostructures.

DOI: 10.1103/PhysRevB.78.174419 PACS number(s): 75.10.−b, 71.30.+h

I. INTRODUCTION

$LaMnO_3$ crystallizes in a structure closely related to the basic ABO_3 perovskite form. As the temperature is varied it undergoes orbital ordering and antiferromagnetic (AFM) transitions. Replacing some of the La with divalent alkali ions such as Ca yields an even wider range of phenomena, including charge ordering, ferromagnetism, and colossal magnetoresistance (CMR).[1–3] The phase diagram is summarized in Fig. 1. While the manganites have been studied for many years and much of the physics has been understood, there is as yet no consensus in the literature on a model which is rich enough to account for all the physics, includes all of important interactions, and can be solved to predict (or at least explicate) new phenomena such as those occurring in systems such as heterostructures. In this paper we develop such a model and explore its properties. Our results place the materials slightly on the insulating side of the Mott metal-insulator phase boundary. We refer to this as the "intermediate-strong" coupling regime.

The phase diagram shown in Fig. 1 includes two magnetic orders, A-AFM and ferromagnetic FM states, corresponding to the Mn spin arrangements shown in Fig. 2. The A-AFM structure consists of ferromagnetic planes antiferromagnetically coupled. With our coordinate choice, each FM plane is spanned by $\hat{x}$ and $\hat{y}$ while the remaining direction is $\hat{z}$. The orbital order in this context refers to a particular distortion arrangement where the oxygen octahedra have in-plane staggered (x-y plane) Q_x Jahn-Teller (JT) distortions plus a uniform $-Q_z$ distortion (the minus sign represents the octahedron shrinking in z while expanding in x-y directions) (Fig. 2). The metal (M)/insulator (I) phase boundary is determined from the dc resistivity. The definition of metal or insulator is ambiguous. Here we adopt the definition that the system is metallic or insulating at a given *temperature* if the temperature derivative of resistivity is positive or negative, respectively.

In this paper, we present a model which captures all of the physics discussed above and solve it by using the single-site dynamical mean-field theory (DMFT).[4] There are two main purposes for this study. First, although basic understanding for exhibited phases at a *given* doping is known, it is important to determine the extent to which the general model with a fixed set of parameters matches the observed phase diagram. Second, we wish to apply this theory to understand the behavior of the recently synthesized manganite superlattices.[5,6]

Solving a theoretical model ordinarily requires approximations. Here we use the single-site DMFT.[4] This approximation requires as an intermediate step the solution of a quantum impurity model. In this paper we solve the impurity model using a generalization of the semiclassical approximation (SCA).[7] We generalize it to the two-band case and develop a formalism for incorporating the cooperative JT effect into the single-site DMFT. We semiquantitatively reproduce the observed phase diagram for $0 < x < 0.5$ and identify the sources of the observed phases. Our calculation yields three main results. First, our calculation suggests that the problem is in the strong-intermediate coupling regime in the sense that under the single-site DMFT approximation the local interaction strength is slightly larger than the critical value needed to drive a metal-insulator transition. Consequently the system is very sensitive to the mechanisms governing the bandwidth such as magnetic order and details of crystal structure. Second, the cooperative Jahn-Teller effect is the main source accounting for the observed high orbital-

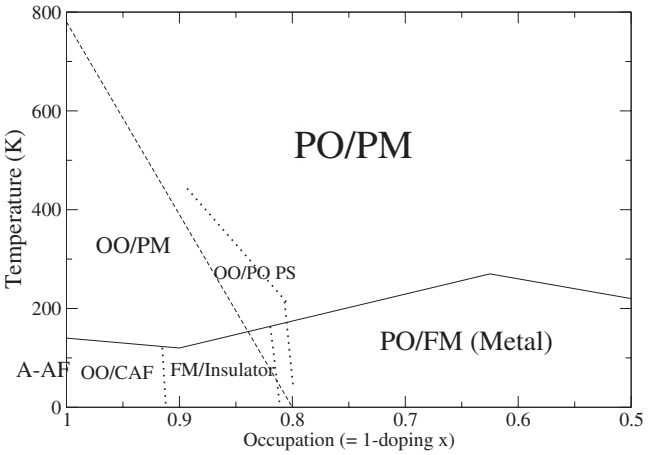

FIG. 1. The experimental phase diagram as a function of doping x and temperature T. PO: paraorbital; PM: paramagnetic; FM: ferromagnetic; OO: orbitally ordered; A-AFM: A-type antiferromagnetic. See text for the descriptions of the phases.

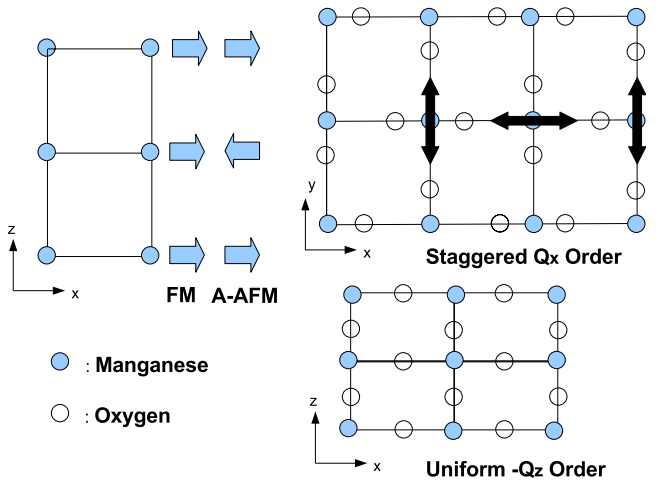

FIG. 2. (Color online) Illustrations of FM, A-AFM, and orbital orders. The filled and open circles represent manganese and oxygen, respectively. The light arrows stand for the core-spin orientation at each plane. Upper left panel: Illustration of two magnetic orders. For FM, the spins at different planes are aligned in the same direction, while for A-AFM, the spins at adjacent planes are arranged oppositely. Upper right panel: Illustration of the in-plane staggered Q_x order. The double arrows represent the long O-Mn-O distance caused by the Q_x distortion. Lower panel: Illustration of the uniform $-Q_z$ order. The system uniformly shrinks in the z direction while it expands in x-y.

ordering temperature. Finally, our calculation confirms that when the doping is increased to the CMR region $x \sim 0.3$ ($N \sim 0.7$), the double-exchange (DE) mechanism becomes dominant.

The rest of the paper is organized as follows. We first present the model and the interactions included. After providing key steps for our approximation, we show how we fit parameters and then present the results. Discussion concerning the inadequacies of our model or approximation and differences between the calculation and the experiments is given in Sec. VII. Section VIII is a conclusion. In Appendixes A and B we examine the validity of the SCA and give details of the procedure we use to take the cooperative Jahn-Teller effect into account.

II. MODEL HAMILTONIAN

In this section we describe the interactions included in our model and define terms and notations which shall be used for the rest of the paper.

A. Tight binding

The band structure is described by a tight-binding model where only nearest-neighbor hopping between e_g orbitals is included. A justification for this approximation is given in Ref. 8. Two e_g orbitals are labeled as $|1\rangle = |3z^2 - r^2\rangle$ and $|2\rangle = |x^2 - y^2\rangle$. This implies a band Hamiltonian which may be written as

$$H_{\text{band}} = \sum_{\vec{k},ab,\sigma} \epsilon_{\vec{k},ab,\sigma} c^{\dagger}_{\vec{k},a,\sigma} c_{\vec{k},b,\sigma}. \tag{1}$$

$\epsilon_{\vec{k},ab,\sigma} = -t(\varepsilon_0 \hat{e} + \varepsilon_z \hat{\tau}_z + \varepsilon_x \hat{\tau}_x)_{ab}$, where $\hat{\tau}$ are Pauli matrices, $\hat{e}$ is the unit matrix and $\varepsilon_0 = \cos k_x + \cos k_y + \cos k_z$, $\varepsilon_z = \cos k_z - \frac{1}{2}(\cos k_x + \cos k_y)$, and $\varepsilon_x = \frac{\sqrt{3}}{2}(\cos k_x - \cos k_y)$. a and b label orbitals, i and j label sites, and σ label spins. We emphasize that what are denoted here as two e_g orbitals are actually the antibonding combination of Mn $3d$ and its neighboring oxygen $2p$ (σ-bond) states.[8]

B. On-site electron-electron

For the on-site interaction within e_g orbitals, we use the Goodenough-Kanamori-Slater approximation in which the form of interaction is the same as in the free atom. Two independent parameters conventionally denoted as U and J are required to specify this interaction. It is generally accepted[9] that the charging energy U may be strongly renormalized by solid-state effects, whereas the interorbital-exchange energy J is less affected. The electron-electron (e-e) interaction within the e_g multiplet is

$$H_{\text{e-e}} = \sum_{\sigma,\sigma'} (U - J) n_{1,\sigma} n_{2,\sigma'} + U \sum_{i=1,2} n_{i,\uparrow} n_{i,\downarrow} + J(c^{\dagger}_{1,\uparrow} c^{\dagger}_{1,\downarrow} c_{2,\downarrow} c_{2,\uparrow} + \text{H.c.}) - 2J\vec{S}_1 \cdot \vec{S}_2, \tag{2}$$

where $\vec{S}_{1(2)} = \vec{\sigma}_{\alpha\beta} c^{\dagger}_{1(2),\alpha} c_{1(2),\beta}$. The $J(c^{\dagger}_{1,\uparrow} c^{\dagger}_{1,\downarrow} c_{2,\downarrow} c_{2,\uparrow} + \text{H.c.})$ term is referred to as the pair hopping and the $-2J\vec{S}_1 \cdot \vec{S}_2$ term is the exchange.

C. Hund's coupling

The coupling between Mn e_g and Mn t_{2g} electrons is approximated by H_{Hund} in which three t_{2g} electrons are treated as an electrically inert "core spin" of magnitude $S = (3/2)\hbar$. We shall further approximate the core spin as classical and normalize J_H by taking $|\vec{S}| = 1$, leading to

$$H_{\text{Hund}} = -J_H \sum_i \vec{S}_i \cdot c^{\dagger}_{i,\alpha} \vec{\sigma}_{\alpha\beta} c_{i,\beta}, \tag{3}$$

where $J_H > 0$ and $|\vec{S}| = 1$. The minus sign ensures that the high-spin state is energy favored in accordance with Hund's rule.

D. Lattice elastic energy

For the lattice degree of freedom, we consider Mn motions in arbitrary directions ($\vec{\delta}_i$) and oxygen only along Mn-O (σ) bond direction ($u_{i,x}$) (Refs. 10 and 11) where $\vec{\delta}_i$ and $u_{i,x}$ are illustrated in Fig. 3. The general lattice elastic energy in the harmonic approximation is

$$H_{\text{lat}} = \frac{1}{2K_{\text{Mn-O}}} \sum_{i,a} [(\delta^a_i - u^a_i)^2 + (\delta^a_i - u^a_{i-a})^2] \tag{4}$$

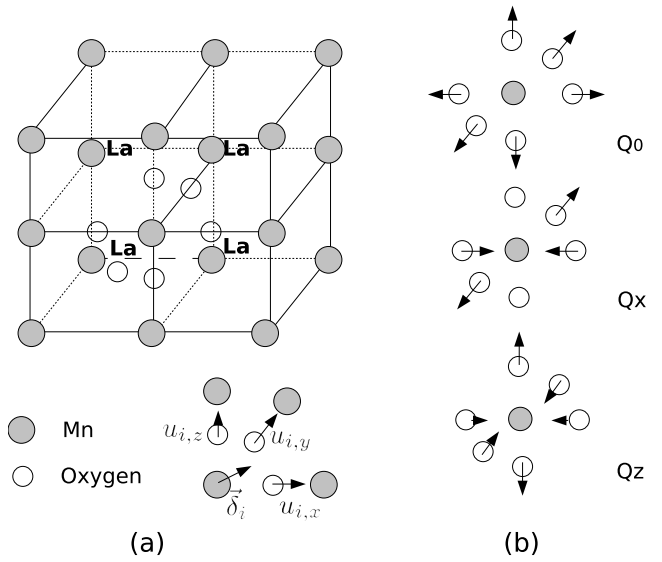

FIG. 3. (a) The ideal cubic perovskite structure for $LaMnO_3$ and the lattice degrees of freedom considered here: Mn can move in arbitrary direction $\vec{\delta}_i$, while oxygen ions only move along the Mn-O bond direction $u_{i,x(y,z)}$. (b) Sketches of the three octahedral distortion modes considered here: Q_0 breathing mode and Q_x and Q_z Jahn-Teller modes.

$$+\frac{1}{2}\sum_{\vec{k},ab} E^{ab}(\vec{k})\delta^a_{\vec{k}}\delta^b_{-\vec{k}} + \frac{1}{2}\sum_{\vec{k},ab} D^{ab}(\vec{k})u^a_{\vec{k}}u^b_{-\vec{k}}, \tag{5}$$

where $1/K_{\text{Mn-O}}$ is spring constant between neighboring manganese and oxygen, while $E^{ab}(\vec{k})$ and $D^{ab}(\vec{k})$ are general Mn-Mn and O-O couplings in k space. In the specific numerical calculations presented here, we set $E^{ab}(\vec{k})=0$ and $D^{ab}(\vec{k})=\frac{4}{k_{\text{Mn-Mn}}}\delta^{ab}\sin^2(k_a/2)$, but effects arising from a more general interaction are discussed. With our convention, u, $\vec{\delta}$, and lattice constants K all have dimension of energy.

E. Electron-lattice coupling

The breathing (Q_0) and JT (Q_x, Q_z) modes at site i are defined by

$$Q_{i,0} = \frac{1}{\sqrt{3}}(v_{i,x} + v_{i,y} + v_{i,z}),$$

$$Q_{i,x} = \frac{1}{\sqrt{2}}(v_{i,x} - v_{i,y}),$$

$$Q_{i,z} = \frac{1}{\sqrt{6}}(-v_{i,x} - v_{i,y} + 2v_{i,z}), \tag{6}$$

where $v_{i,a}=u_{i,a}-u_{i-a,a}$. The e_g orbitals couple to these three modes as

$$H_{\text{JT}} = -\sum_{i,a,b}(Q_{i,x}\tau^x_{ab} + Q_{i,z}\tau^z_{ab})c^\dagger_{i,a}c_{i,b}, \tag{7}$$

$$H_B = -\beta Q_{i,0}(n_i - \langle n\rangle), \tag{8}$$

where β is dimensionless and positive. We will take $\beta=1$, which simplifies the discussion of cooperative Jahn-Teller effect. In this paper we treat H_B by a mean-field approximation, so it is only important when the charge distribution is not uniform, such as in the heterostructures or in the charge-ordered (CO) phase. In our definition, positive Q_z stands for the distortion where the octahedron *expands* in the z direction while *shrinking* uniformly in x-y with fixed volume. The minus sign in Eq. (7) means that the positive Q_z favors the occupancy of the $|3z^2-r^2\rangle$ state. This sign choice is justified because positive Q_z increases the lattice constant in the z direction and consequently reduces $|t_{pd}|$ and $E_{\text{antibonding}}$, increasing the occupation in the antibonding band which is mainly composed of Mn $|3z^2-r^2\rangle$. A similar consideration leads to the minus sign in Eq. (8) (positive Q_0 means a volume expansion of the octahedron).

F. Cubic term in lattice energy

An anharmonic cubic term[12] in lattice energy is also included,

$$H_{\text{Cubic}} = -A(3Q^3_{i,z} - Q^2_{i,x}Q_{i,z}), \tag{9}$$

where A in our convention has the dimension $[E]^{-2}$. Note this is the only cubic combination satisfying the lattice cubic symmetry. With the minus sign, positive A is required to produce the observed distortions for $LaMnO_3$.

G. G-type AFM coupling

There is an isotropic nearest-neighbor AFM coupling (G-type) between t_{2g} spins $\vec{S}_i$,

$$H_{\text{AFM}} = J_{\text{AFM}}\sum_{i,\hat{n}} \vec{S}_i \cdot \vec{S}_{i+\hat{n}}, \tag{10}$$

with positive J_{AFM}. This coupling arises from the superexchange (SE) mechanism (virtual hopping in t_{2g} channels) and experimentally shows in the G-type antiferromagnetic (G-AFM) order exhibited in $CaMnO_3$.[2] The main effect of this term is to reduce the magnetic transition temperature. The total Hamiltonian is then

$$H_{\text{tot}} = H_{\text{band}} + H_{\text{e-e}} + H_{\text{Hund}} + H_{\text{lat}} + H_{\text{JT}} + H_B + H_{\text{Cubic}} + H_{\text{AFM}}. \tag{11}$$

III. METHOD

We use the single-site DMFT with the SCA to solve this two-orbital problem.[7] In the DMFT approximation one replaces the full lattice self-energy $\Sigma(\omega,\vec{p})$ by a local (momentum-independent) quantity $\Sigma(\omega)$ which is determined from the solution of an auxiliary problem (quantum impurity model) plus a self-consistency condition. The multiplicity of orbitals and interactions means that the impurity model is not easy to solve. We use a Hubbard-Strotonovich (HS) transformation proposed by Sakai *et al.*[13] and the semiclassical approximation. To evaluate the frequency sum, we

use a procedure recently introduced by Monien.[14]

We also mention two simplifications here. First we do not take into account the Coulomb potential produced by the random distribution of cations—the only effect of replacing some La with divalent elements is to reduce the e_g electron population. However due to the screening effect from conduction electrons, we believe this simplification is not crucial. Second, we restrict our calculation to charge-uniform states. Therefore we cannot obtain the charge-ordered phase which may be energy favored around half doping.

The rest of this section is organized as follows. Two key ingredients will be discussed: first we show how we encode the cooperative Jahn-Teller effect in the local impurity problem; second we give some detailed formalism about SCA in this two-orbital problem, especially how we decompose the quartic interaction and what simplifications we make. Then we discuss what measurements we use to fit parameters.

A. Cooperative Jahn-Teller

The local octahedral distortions (Q_0, Q_x, Q_z) at different sites are not independent—distortion at one site inevitably causes distortion at the neighboring sites so that some global configurations of the lattice distortions are energy favored. This is the cooperative Jahn-Teller effect[10] which correlates the octahedral distortions at different sites. Here we include this intersite effect into the single-site DMFT by integrating out all of distortion fields except for those involving the variable v at the site of interest. The detailed calculation is given in Appendix B and the resulting local effective potential is

$$V_{\text{eff}}(Q_0, Q_x, Q_z) = \frac{Q^2}{2K} + \epsilon \vec{F} \cdot \vec{Q}, \tag{12}$$

where K is an effective spring constant and $\epsilon\vec{F}$ represents the force exerted on the distortions at one site by static (mean-field) distortions on the other site. Here $\vec{F}$ measures the amplitude of the long-ranged order and ϵ gives the strength of the cooperative Jahn-Teller coupling.

B. On-site e-e

The key step in our solution of the impurity model is to rewrite the quartic interaction into sums of complete squares so the continuous Hubbard-Strotonovich transformations can be applied. Using the decomposition proposed by Sakai *et al.*,[13] we define $f_\sigma \equiv c_{1\sigma}^\dagger c_{2\sigma} + c_{2\sigma}^\dagger c_{1\sigma}$, $n \equiv n_1 + n_2$, $q \equiv n_1 - n_2$, $s \equiv (n_{1,\uparrow} - n_{1,\downarrow}) + (n_{2,\uparrow} - n_{2,\downarrow})$, and $d \equiv (n_{1,\uparrow} - n_{1,\downarrow}) - (n_{2,\uparrow} - n_{2,\downarrow})$, and re-express Eq. (2) as

$$H_{\text{e-e}} = U_0 n - \frac{J}{2}(f_\uparrow - f_\downarrow)^2 + \frac{U_n}{2}n^2 - \frac{U_q}{2}q^2 - \frac{U_s}{2}s^2 - \frac{U_d}{2}d^2, \tag{13}$$

with $U_0 = 0$, $U_n = (3U - 5J)/4$, $U_q = (U - 7J)/4$, $U_s = (U + J)/4$, and $U_d = (U - 3J)/4$. Due to the fermionic identity $\hat{n}_{i,\sigma}^2 = \hat{n}_{i,\sigma}$ $(i = 1, 2;\ \sigma = \uparrow, \downarrow)$, those coefficients are not unique. For example, $U_0 = J/2$, $U_n = (3U - 6J)/4$, $U_q = (U - 6J)/4$, $U_s = (U + 2J)/4$, and $U_d = (U - 2J)/4$ is another legitimate set of choices. If the impurity problem is solved exactly, these two choices lead to the same result; but if approximate methods are used, this need not be the case. However in the current study, the coefficients will be determined by fitting to data so this ambiguity is not important.

C. Impurity problem

The impurity problem is then described by the effective action $S = S_0 + S_{\text{int}}$, where

$$S_0 = -\int d\tau d\tau' a_{\alpha\beta}^{ij}(\tau - \tau') c_{\alpha,i}^\dagger(\tau) c_{\beta,j}(\tau') \tag{14}$$

and $S_{\text{int}} = \int d\tau H_{\text{e-e}}(\tau)$. The partition function is $Z_{\text{imp}} = \int d\vec{Q} d\vec{S} D[c^\dagger c] e^{-S}$. Applying the HS transformations[13] to decouple $H_{\text{e-e}}$, one arrives at

$$\begin{aligned} S_{\text{int}} = \int d\tau \Big(& \frac{1}{2U_n}\phi_n^2(\tau) + \frac{1}{2J}\phi_f^2(\tau) + \frac{1}{2U_q}\phi_q^2(\tau) + \frac{1}{2U_s}\phi_s^2(\tau) \\ & + \frac{1}{2U_d}\phi_d^2(\tau) \Big) + \int d\tau \{ -\phi_n(\tau) n(\tau) + \phi_f(\tau)[f_\uparrow(\tau) \\ & - f_\downarrow(\tau)] + [\phi_q(\tau) q(\tau) + \phi_s(\tau) s(\tau) + \phi_d(\tau) d(\tau)] \} \\ & + \int d\tau (\vec{Q} \cdot \vec{T}_{ab} \delta_{\alpha\beta} + J_H \vec{S} \cdot \delta_{ab} \vec{\sigma}_{\alpha\beta}) c_{i,\alpha}^\dagger(\tau) c_{j,\beta}(\tau). \end{aligned} \tag{15}$$

To maintain the symmetries of the local interaction [SU(2) for spin and U(1) for orbital], we generalize the scalars ϕ_s and ϕ_q, to vectors $\vec{\phi}_s$ $[=(\phi_{s,x}, \phi_{s,y}, \phi_{s,z})$, three components] and $\vec{\phi}_q$ $[=(\phi_{q,z}, \phi_{q,x})$, two components] and average over their directions.[15] After expressing the S_{int} in frequency space, two simplifications are made. First, only zero-frequency component for each HS field $[\phi(i\omega_0) = \phi]$ is kept and, second, saddle-point approximations are applied to ϕ_f, ϕ_d, and Q_0 fields, i.e., $\phi_f = \phi_d = Q_0 = 0$. Different methods have been proposed for handling the $i\phi_n$ field.[7,16] For the two-band model studied here, we found that the method in Ref. 7 effectively enhances the local orbital moment as the doping increases, which is opposite of the observation, while the method in Ref. 16 is free from this trouble. Therefore we follow Ref. 16 and take $i\phi_n = 0$. After integrating out the fermionic degree of freedom and combining the lattice effect, one gets

$$\begin{aligned} V_{\text{eff}} = & \left(\frac{Q^2}{2K} + \frac{\phi_q^2}{2U_q} + \frac{\phi_s^2}{2U_s} \right) + A(3\langle Q_z \rangle^2 - \langle Q_x \rangle^2) Q_z + \epsilon \vec{F} \cdot \vec{Q} \\ & - T \sum_{\omega_n} \text{Tr} \log \mathbf{A}(i\omega_n), \end{aligned} \tag{16}$$

with

$$\mathbf{A} = \mathbf{a} + (\vec{Q} + \vec{\phi}_q) \cdot \vec{\tau} + (J_H \vec{S} + \vec{\phi}_s) \cdot \vec{\sigma}, \tag{17}$$

where $\mathbf{A}$ is a 4×4 matrix and $\mathbf{a}$ is the Weiss function. The $A(3\langle Q_z \rangle^2 - \langle Q_x \rangle^2) Q_z$ term comes from the simple mean-field approximation of the cubic lattice energy.

D. Parameters and fitting

The discussion above indicates that there are seven parameters to be determined: the hopping t, effective local JT

coupling U_Q, effective magnetic coupling U_s, Hund's coupling J_H, core-spin AFM coupling J_{AFM}, cooperative JT coefficient ϵ, and anharmonic lattice energy A. The first six have the dimension of energy (E) and will be measured in units of the hopping t, while the last one has dimension $1/E^2$.

The hopping strength t has been determined from the band-structure calculation for the experimentally observed structure of $LaMnO_3$ to be roughly 0.5 eV ($\sim$5000 K).[8] In contrast, the value appropriate to the ideal perovskite structure is roughly 0.65 eV. The difference is due mainly to the effect of the $GdFeO_3$ rotation. For the series $La_{1-x}Ca_xMnO_3$ the distortion depends weakly on the doping x (less than 10%). For $La_{1-x}Sr_xMnO_3$ the rotation angle is more x dependent (up to 30%). Therefore calculations in which t is taken to be independent of x may be appropriate for the Ca series but are unlikely to be adequate for the Sr series. We focus here on the Ca series. We note that the value $t=0.5$ eV is in good agreement with the spectral weight inferred from the optical conductivity experiments on the ferromagnetic phase of $La_{0.7}Ca_{0.3}MnO_3$.[17] The J_{AFM} is estimated from the Néel temperature of $CaMnO_3$, roughly 110 K $\sim$0.01 eV.[2] The T_N of the Heisenberg model $H=\Sigma_{i,j}J_{\mathrm{AFM}}\frac{9}{4}\vec{S}_i\cdot\vec{S}_j$ with $|\vec{S}|=3/2$ obtained from simple mean field is $\frac{20}{9}J_{\mathrm{AFM}}$, from which we estimate $J_{\mathrm{AFM}}\sim 4.5$ meV $\sim 0.009t$. The superexchange argument (from virtual hopping of t_{2g} electrons)[18] also leads to the same estimate. We further found that within the mean-field approximation, the J_{AFM} term only acts to reduce to magnetic transition temperatures by 5–10 % but does not result in any new magnetic order. Including this term however substantially increases the calculation time, so we typically set $J_{\mathrm{AFM}}=0$ to accelerate the converging processes. The anharmonic lattice energy is taken to be $A=0.006t^{-2}$ so that our calculation reproduces the observed JT distortion around room temperature for $LaMnO_3$.[19]

The remaining parameters J_H, U_s, U_Q, and ϵ are fitted by comparing the calculated and observed optical conductivities in $LaMnO_3$. Generally the $\sigma(\omega)$ contains peaks corresponding to local excitation energies of the system. If we treat the hopping t as a small perturbation, then peaks in the optical conductivity are roughly the energy differences between the excited states and the ground state of the *local* Hamiltonian. Since there are four states (2 spins $\times$ 2 orbitals) at each site, we expect there are three main peaks in $\sigma(\omega)$ corresponding to three two-electron final states. The saddle-point estimate from the local potential indicates that these three peaks are located at $2U_Q(1+\epsilon)$ (correct spin, other orbital), $2(J_H+U_s)$, (same orbital, antiparallel spin), and $2U_Q(1+\epsilon)+2(J_H+U_s)$ (other orbital, antiparallel spin) which essentially agrees with our calculated results shown in Fig. 5. The issue is discussed further in Ref. 20. Experimentally there are two apparent peaks observed in $LaMnO_3$ (Ref. 21)—the lower one is around 2 eV ($\sim 4t$), while the higher one is around 4 eV ($\sim 8t$). There are several minor structures around 5–6 eV which we do not consider. Fitting the two main peaks in optical data suggests $U_Q(1+\epsilon)\sim 4(t)$ and $J_H+U_s\sim 8(t)$. We choose $J_H=2.8$, $U_s=1.4$, $U_Q=2.1$, and $\epsilon=0.05$. We found that if J_H+U_s is fixed, the relative values of J_H and U_s do not change the result much as long as $U_Q>U_s$. If $U_Q<U_s$, the orbital order is not stable against the magnetic order. Since at $T=0$ the SCA reduces to the simple mean-field approximation where expectation values are determined by their saddle-point values, the combination $U_Q(1+\epsilon)$ uniquely determines the $T=0$ phase. However ϵ has more significant effect on the nonzero-temperature phase. We choose ϵ so as to produce the observed T_{OO}.

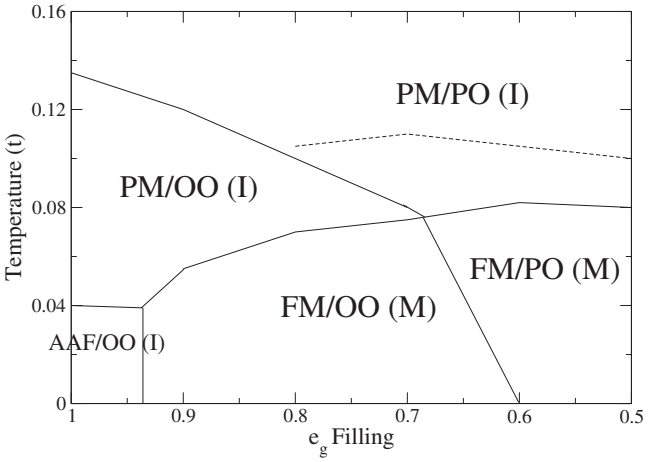

FIG. 4. Calculated phase diagram as a function of doping x and temperature. M and I stand for metallic and insulating phases. The dashed curve is the PM/FM phase boundary, computed using $t=0.6$ eV appropriate to $La_{0.6}Sr_{0.4}MnO_3$.

Standard parametrization

Unless indicated otherwise the results we shall present later correspond to our standard parameters $t=0.5$ eV, $U_Q=2.1t$, $U_s=1.4t$, $J_H=2.8t$, $J_{\mathrm{AFM}}=0$, $\epsilon=0.05$, and $A=0.006/t^2$. We remind the reader that this choice of t is only appropriate for Ca-doped materials; in the Sr series the t changes with doping. All the temperatures and frequencies are measured in t; a simple conversion is 0.5 eV $\sim$ 5500 K.

IV. PHASE DIAGRAM

The calculated phase diagram as a function of doping and temperature is shown in Fig. 4. The results qualitatively reproduce the observed phase diagram (Fig. 1) in the sense that the relative positions of calculated magnetic or orbital phases are consistent with the experiments, but the temperature scales are larger than observed.

According to the doping, we divide the phase diagram into three regions—the undoped case ($x=0$, $LaMnO_3$), the CMR regime ($0.3<x<0.5$), and the crossover regime ($0<x\leq 0.3$). In essence, the undoped case is cooperative JT dominated and the signature is the lattice distortions or equivalently the orbital order. On the other hand, the CMR regime is DE dominated in which the system is FM or metallic at low temperature. In the crossover regime, both mechanisms play non-negligible roles to the system and we see that as doping increases, the cooperative JT effect decreases (T_{OO} decreases) while the DE mechanism gradually takes over (T_C increases). In principle, we can extend our calculation to $x>0.5$. However this region the effect of G-type AFM coupling J_{AFM} starts to emerge (or both double-

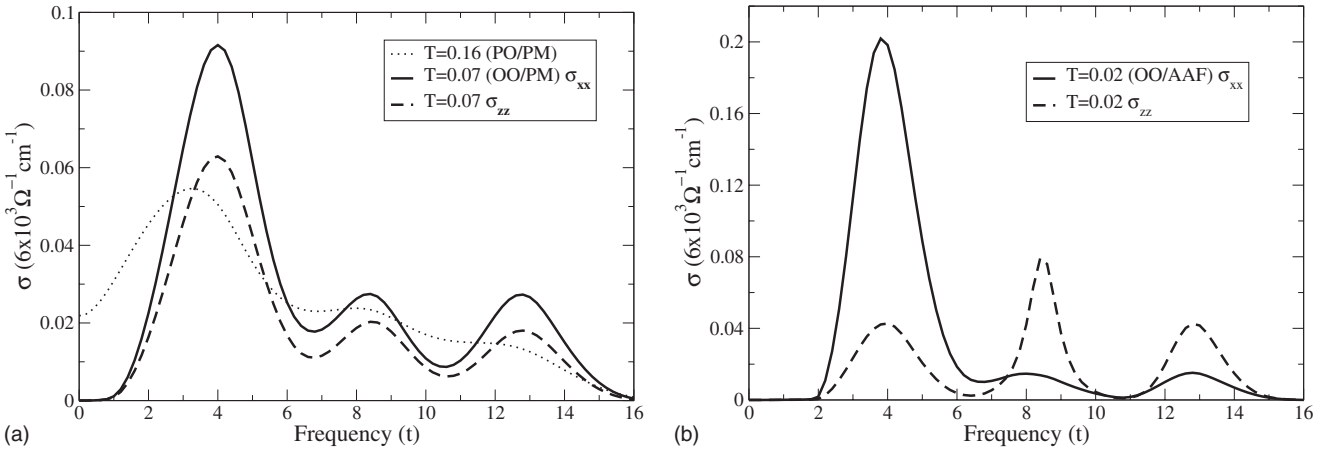

FIG. 5. Optical conductivities for (a) $T=0.16t$ ($>T_{OO}$) (dotted) and $T=0.07\sim0.5T_{OO}$, OO/PM phase, and (b) $T=0.02t\sim0.5T_{A\text{-}AFM}$, OO/A-AFM phase. The heavy solid or dashed curves represent the in-plane or out-of-plane optical conductivities, respectively. To convert the frequency scale to physical units, we note that the band theory indicates $t=0.5$ eV so $t=4$ corresponds to 2 eV.

exchange and cooperative JT effects decrease) and a different self-consistency condition (G-AFM) is required, so we shall leave it for future study.

The remainder of the paper is organized as follows. We shall devote one section for the undoped case and one for the CMR and crossover region for more detailed discussions, then discuss the discrepancies between calculated and observed results. What important physics we are missing in our model or approximation and their effects to the current results will be stated. We also point out here that for the spectral functions we shall present, the Fermi energy is at zero. Without further indications, ρ, σ, and A stand for resistivity, conductivity, and spectral function, respectively.

V. UNDOPED CASE

A. Overview

Experimentally $LaMnO_3$ is insulating for all temperatures at least up to 800 K,[21–23] which is slightly greater than the orbital-ordering temperature T_{OO}. When the temperature is lowered, it first goes from PO/PM to OO/PM at $T_{OO}\sim780$ K $(0.135t)$, then from OO/PM to OO/AFM at $T_{A\text{-}AFM}\sim140$ K $(0.04t)$, where temperatures in kelvins are experimentally derived while numbers in parentheses are from calculation. After a discussion about the nature of the insulating behavior, we examine the physical origins of the exhibited phases.

B. Transport and excitation spectrum

In this subsection we present our calculated optical conductivities for the stoichiometric end member $LaMnO_3$. We show that the calculated conductivities are in good agreement with experiment and that the agreement implies that $LaMnO_3$ is a Mott insulator. A more careful discussion regarding Mott insulator is given in Ref. 20.

To establish our claim we present in Fig. 5 the optical conductivities for electric fields parallel to the x-y plane (solid line) and perpendicular to it (dashed line) at temperatures $T=0.16t$ (greater than T_{OO}), $T=0.07t$ (below T_{OO}, above the magnetic-ordering temperature $T_{A\text{-}AFM}$), and $T=0.02t$ (roughly $0.5T_{A\text{-}AFM}$). The integrated optical conductivities up to 3 eV qualitatively agree with experiments on $LaMnO_3$.[23] At $T=0.16t$ we see that the conductivity has two peaks at $\omega\sim4t$ and $8t$, and a soft gap at $\omega=0$. If we suppress the orbital order, forcing PO/PM solution down to lower temperature, we find that the low-frequency conductivity decreases.[20] When the temperature is lowered to $T=0.07t$, where the orbital order is well established, the peak positions remain essentially unchanged. An anisotropy produced by the orbital order appears and the gap at low frequency becomes sharper.

As the temperature is further decreased into the A-type antiferromagnetic state, the peaks sharpen and the anisotropy becomes more pronounced with an increase in σ_{xx} and a decrease in σ_{zz} for $\omega\sim4t$; the converse behavior occurs in the $\omega\sim8t$ regime. This qualitative behavior was used by authors of Refs. 21 and 24 to identify the lower feature as the transition to the maximal-spin, orbitally disfavored final state and the higher feature as the transition to a lower-spin, orbitally favored state. We make the same identification here and have adjusted the crucial parameters U_Q and U_s to place these peaks at the experimentally correct energies. Referring now to Fig. 5(a), we see that for these parameters the correlations are already strong enough to produce an insulating state in the absence of the long-ranged order which is one characteristic of Mott insulator, although the "soft" nature of the gap places the materials close to the Mott insulator/metal phase boundary.

C. Origins of exhibited phases

Along the temperature-descending direction, we summarize our understanding with the following statements:

(1) The staggered Q_x order is a consequence of the cooperative JT effect, i.e., a combined effect from local JT interaction and lattice elastic energy.

(2) The energy difference between (π,π,π) Q_x and $(\pi,\pi,0)$ Q_x orders is very small, on the order of meV.

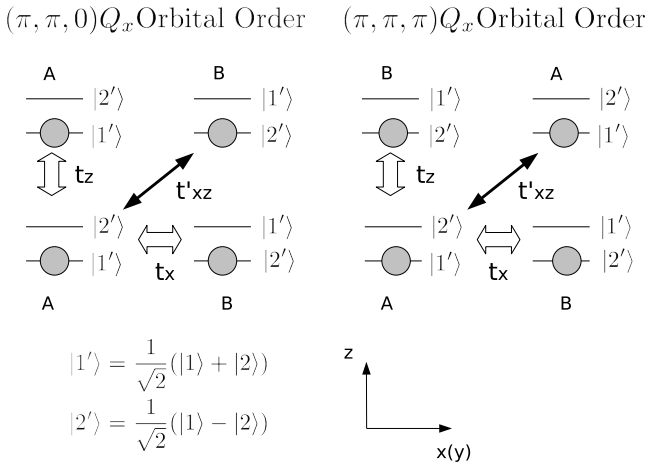

FIG. 6. Illustrations of superexchange processes in the presence of different $(\pi,\pi,0)$ and (π,π,π) Q_x orbital orders. A and B are two sublattices occupying local orbitals $(|1\rangle+|2\rangle)/\sqrt{2}$ and $(|1\rangle-|2\rangle)/\sqrt{2}$, respectively. The hopping matrices are directional and the explicit forms are given in Ref. 8.

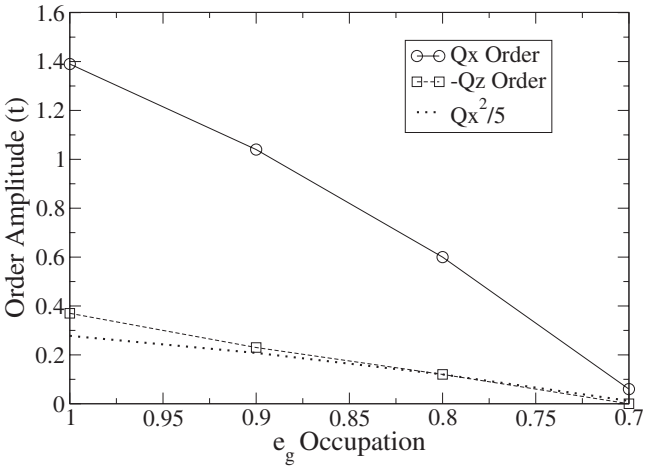

FIG. 7. The staggered Q_x (solid curve) and the uniform Q_z (dashed curve) orders as functions of doping at $T=0.1t$. In the bulk, the uniform $-Q_z$ order is induced by the cubic term in lattice energy and the magnitude is proportional to Q_x^2. For the chosen parameters here $Q_z \sim 0.2Q_x^2$ (dotted curve).

(3) The uniform Q_z order is a consequence of the staggered Q_x order, arising from the cubic term in lattice energy.

(4) The uniform $-(+)Q_z$ order reduces (enhances) the interlayer AF coupling and decreases (increases) the Néel temperature.

To justify the first statement, we perform the calculation without cooperative Jahn-Teller effect and obtain an orbital-ordering temperature of $0.06t$ ($\sim$330 K), which is far too low compared to the observation. The cooperative Jahn-Teller coupling arising from the corner-shared octahedra facilitates the staggered Q_x order. The physical picture is quite straightforward—a Q_x distortion on one site induces a $-Q_x$ distortion on neighboring sites on the same x-y plane.

The second statement concerns the energy difference between the $(\pi,\pi,0)$ and the (π,π,π) Q_x orders. There are two possible sources. The first one is the structure in the lattice contribution. The simple form of the lattice Hamiltonian[25] we used in our numerical calculation has the same restoring force for both distortions, but a more general form given in Eq. (5) will distinguish them. Assessing this possibility requires a density functional theory (DFT) calculation of phonon spectrum as is discussed in Ref. 25. The second possibility is the electronic energy, which we now estimate from the SE (essentially second-order perturbation) argument. The nearest-neighbor (t) and second-neighbor (t') hopping processes which give rise to superexchange are illustrated in Fig. 6.

In terms of the local JT splitting of Δ_Q, we find that the second-order superexchange calculation yields that the energy gain for both orders is $-\frac{9}{4}\frac{t^2}{\Delta_Q}$. Therefore within SE approximation, nearest-neighbor hopping does not lift the degeneracy. However the second-neighbor hopping does lift the degeneracy. We find that the $(\pi,\pi,0)$ Q_x state gains $-4\frac{t'^2}{\Delta_Q}$ more energy than the (π,π,π) state. From our DFT study,[8] $t' \sim 0.035$ eV and $\Delta_Q \sim 1.4$ eV. Therefore the energy difference between these two orders is on the order of meV, which is very small compared with other energy scales in the problem. We therefore believe that the lattice effect is dominant. We model this by allowing only the $(\pi,\pi,0)$ order in our calculation.

Within our approximation, the uniform Q_z order is induced by the *local* Q_x distortion via the cubic term[12] in lattice energy, so the strength of the Q_z order is proportional to Q_x^2. Figure 7 shows the magnitudes of the staggered Q_x and uniform Q_z orders at $T=0.1t$. For these parameters we found $Q_z \sim 0.2Q_x^2$.

The fourth statement concerns the relation between the magnetic order and orbital order. In particular it is the answer to the question of how in the presence of a large staggered Q_x order a small uniform Q_z order affects the magnetic order. We found that a small $\pm Q_z$ order can change the Néel temperature $T_{\text{A-AFM}}$ by as much as a factor of 2. This effect can be qualitatively understood by comparing the effective magnetic couplings J_i ($i=z$ out of plane and x in plane) for different orbital orders using superexchange arguments. The starting point is that for each site the electron occupies the orbital $|\theta\rangle \equiv \cos\theta|1\rangle + \sin\theta|2\rangle$ $(0<\theta<\pi)$ which is the ground state of $-(Q_z\hat{\tau}_z + Q_x\hat{\tau}_x)$. Since the strength of Q_x order is at least three times larger than that of Q_z order (see Sec. II G), we consider $Q_z/|Q_x|$ ranging from -0.3 to 0.3. As shown in Fig. 8 in the presence of the staggered Q_x order, the system is divided into two sublattices A and B on which the electron occupies orbital $|\theta_A\rangle$ and $|\theta_B\rangle$. Defining $\cos 2\theta = Q_z/\sqrt{Q_x^2+Q_z^2}$ and $\sin 2\theta = Q_x/\sqrt{Q_x^2+Q_z^2}$, one finds that the occupied orbitals at A and B are $|\theta\rangle$ and $|-\theta\rangle$. Using the second-order perturbation, one estimates the magnetic couplings from the energy difference between FM and AFM spin configurations ($J=E_{\text{FM}}-E_{\text{AFM}}$) as

$$J_z(\theta) = -\frac{\cos^2\theta\sin^2\theta}{\Delta_{\text{JT}}} + \frac{\cos^4\theta}{\Delta_{\text{Hund}}} + \frac{\cos^2\theta\sin^2\theta}{\Delta_{\text{Hund}}+\Delta_{\text{JT}}},$$

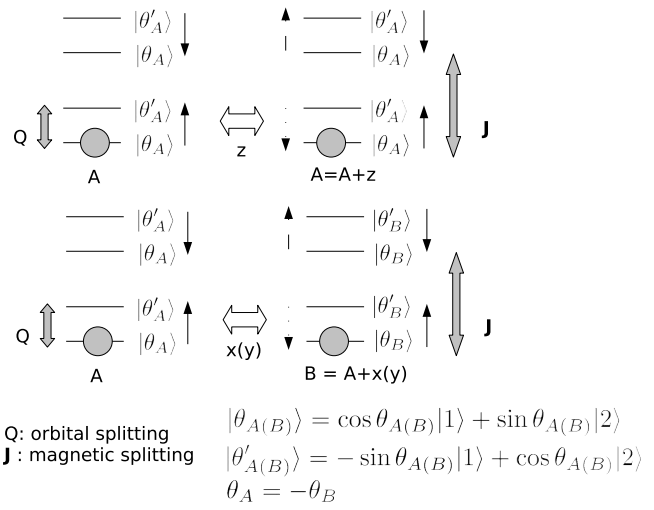

$$|\theta_{A(B)}\rangle = \cos\theta_{A(B)}|1\rangle + \sin\theta_{A(B)}|2\rangle$$
$$|\theta'_{A(B)}\rangle = -\sin\theta_{A(B)}|1\rangle + \cos\theta_{A(B)}|2\rangle$$
$$\theta_A = -\theta_B$$

FIG. 8. Illustration of the $(\pi,\pi,0)$ Q_x and a uniform Q_z orbital order. The local orbital states are same in the z direction ($|\theta_A\rangle$ or $|\theta_B\rangle$), while they are alternate between $|\theta_A\rangle$ and $|\theta_B\rangle$ on the x-y plane.

$$J_x(\theta) = -\frac{3/16 + \cos^2\theta \sin^2\theta}{\Delta_{\mathrm{JT}}} + \frac{\cos^2\theta - 3\sin^2\theta}{4\Delta_{\mathrm{Hund}}} + \frac{3/16 + \cos^2\theta \sin^2\theta}{\Delta_{\mathrm{Hund}} + \Delta_{\mathrm{JT}}}, \quad (18)$$

where Δ_{JT} and Δ_{Hund} are orbital and magnetic splittings, respectively. From previous discussion we found $\Delta_{\mathrm{JT}} \sim 2$ eV $\sim 4t$ and $\Delta_{\mathrm{Hund}} \sim 4$ eV $\sim 8t$. The corresponding results are given in Fig. 9, where $\theta/\pi = 0.2, 0.25, 0.3$ correspond to $Q_z/|Q_x| = +0.3, 0, -0.3$, respectively. We see that for these θ values the in-plane magnetic coupling is always FM, while the out-of-plane changes from FM to AFM when θ/π varies from 0.3 to 0.2 (zero coupling at $\theta = 0.22\pi$). This SE estimate therefore implies that a positive Q_z order is required to produce the observed A-AFM order. In our DMFT calculation, we always find the A-AFM order at low temperature, but we indeed find that the Néel temperature drastically (50%) increases when we go from small $-Q_z$ to small $+Q_z$ order. Thus the trend of variation in T_N with strain is correctly captured by the superexchange calculation, but other processes also contribute the overall sign. This result indicates that the interaction is not strong enough to justify the superexchange approximation but that the superexchange results do capture one aspect of the important physics.

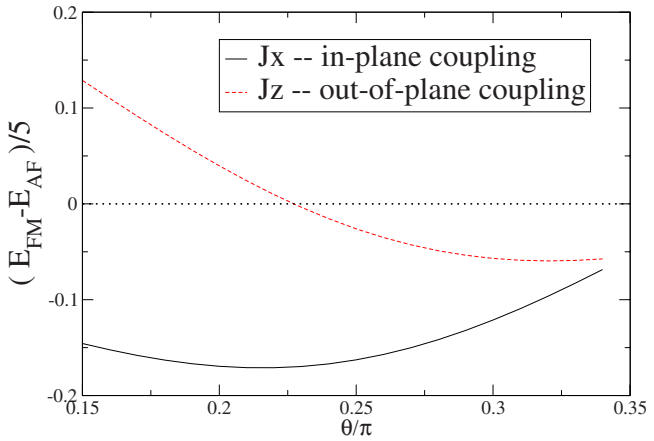

FIG. 9. (Color online) The out-of-plane (J_z) and in-plane (J_x) magnetic couplings estimated from Eq. (18) with $\Delta_{\mathrm{JT}} = 4t$ and $\Delta_{\mathrm{Hund}} = 8t$. The negative sign favors FM coupling. $\theta = 0.25\pi$ represents the case without uniform Q_z order. Positive and negative Q_z orders correspond to the region $\theta < \pi/4$ and $\theta > \pi/4$, respectively.

VI. CMR REGIME AND CROSSOVER

A. CMR regime ($0.3 < x < 0.5$)

We choose $x = 0.3$ ($N = 0.7$) as being representative of the CMR region. For this doping, the system goes from PO/PM to PO/FM around 275 K. The transition is accompanied by an insulator/metal transition which is shown in Fig. 1 of Chapter 1 of Ref. 26. At this transition the $d\rho/dT$ changes sign. Figure 10(a) shows the calculated $\rho(T)$. We indeed find a M/I transition across the Curie transition. This M/I transition is also reflected in the optical conductivities shown in

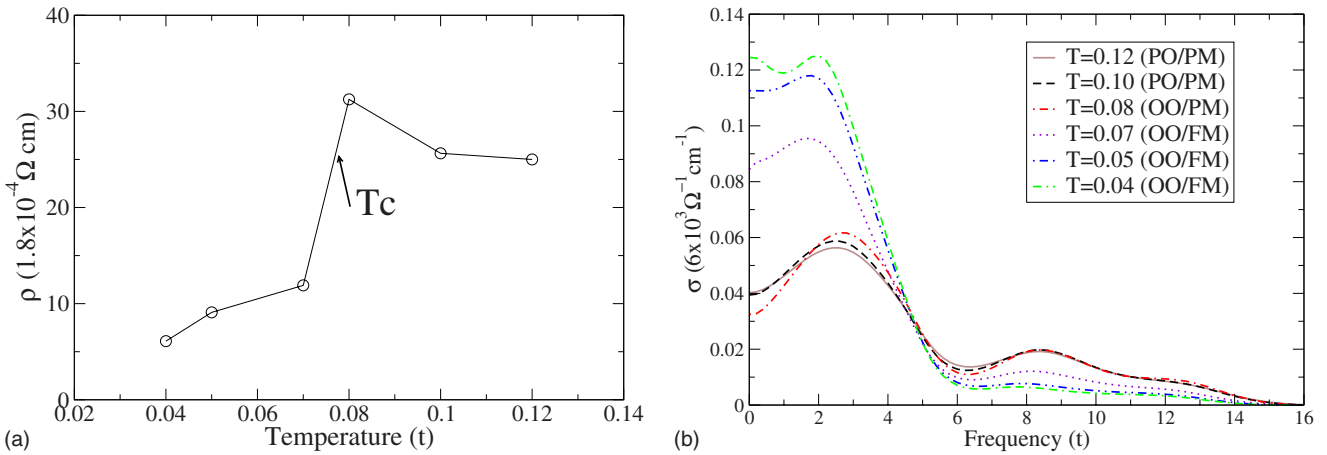

FIG. 10. (Color online) (a) In-plane dc resistivity $\rho_{xx}(T)$ as a function of temperature for $x = 0.3$. (b) In-plane optical conductivities for $x = 0.3$ and $T = 0.12t - 0.04t$.

TABLE I. Kinetic energies in eV obtained from both experiments and our calculation, using $t=0.5$ eV.

	Expt. (Ref. 17)	Calc.
FM	0.22	0.152 ($T=0.04t$)
PM	0.1	0.076 ($T=0.1t$)

Fig. 10(b). Our calculations qualitatively agree with the experimental data on $La_{0.7}Ca_{0.3}MnO_3$. To be more quantitative, Table I compares the kinetic energy defined as $K=(\frac{\hbar a}{e^2})\frac{2}{\pi}\int_0^{2.7\ \mathrm{eV}}\sigma(\omega)d\omega$ obtained from both experiments[17] and our theoretical calculation. The reasonable agreement suggests that our model well captures the main physics (right degree of freedom and reasonable effective interactions) below 2.7 eV. However there are several differences between calculation and data. First the experimental values are systematically larger. Two reasons are that the experiments inevitably involve transition from lower oxygen bands to Fermi level which is not included in our model and our calculation yields orbital order at low T which does not occur in the actual material. In addition our calculation overestimates the density of states around zero frequency at high-temperature PM phase. In terms of dc resistivity, this means that the high-T PM phase is not insulating enough. We shall discuss the possible physics accounting for this inconsistency later.

One issue from earlier calculations is that the T_C for pure DE model is roughly three times higher than the observed one.[27] The Curie temperature T_C with $J_{\mathrm{AFM}}=0$ obtained here (roughly $0.08t$) is ~40% lower than that of Ref. 27. Introducing G-type AFM coupling J_{AFM} (~$0.01t$ from our fit) further reduces T_C to $0.075t\sim 412$ K, not too far from the experimental value of ~275 K. We expect that a large fraction of the remaining difference arises from spatial and thermal fluctuation effects not captured by our mean-field theory.

B. Crossover regime ($0.1<x<0.3$)

In this doping range, when the temperature is lowered, the system goes from PO/PM to OO/PM, then to OO/FM phase and we take $x=0.2$ ($N=0.8$) as a representative doping. In this region, both cooperative JT and DE mechanisms are important. These two mechanisms are competing and not compatible in the following sense—the cooperative JT tends to break the in-plane symmetry which facilitates the staggered Q_x order and localizes electrons, while the DE wants the system to be uniform and delocalizes electrons. This competition is shown in Fig. 11(a), where the magnitude of the staggered Q_x order is plotted. We find that when lowering the temperature, the magnitude of Q_x order increases above the Curie temperature, and then quickly saturates below T_C. If we force the PM solution at low temperature, then the staggered Q_x order keeps on increasing as T is decreased. This is consistent with the pair distribution function (PDF) measurements[28] which show that below the Curie temperature at $x=0.25$, the peak associated with JT distortion decreases when lowering the temperature. Figure 11(b) shows the resistivity as a function of temperature. We see that the system is an insulator at high temperature and a downturn in $\rho(T)$ happens at the Curie temperature, below which DE effects gradually take over and the system is metallic. Finally we point out that around $x=0.3$, T_{OO} and T_C happen around the same temperature (around $0.1t$ in Fig. 4). We do not resolve the behavior around this point carefully.

VII. DISCUSSION

A. Summary

With a fixed set of parameters, our calculations semiquantitatively produce the observed phase diagram—the relative positions of magnetic and orbital orders on the doping-temperature plane are consistent with experiments. In particular the magnetic transition temperatures (both Néel and Curie temperatures) are in reasonable agreement with data, with calculated values being about 1.5 times higher than the measured values. Some part of the difference arises from the fluctuation corrections to the mean-field theory, which are typically on the order of 30% in three dimensions. As for the excitation spectra, our results are consistent with observed optical conductivity. In particular we reproduce the peak positions (this is how we fit some of the parameters) and the corresponding amplitudes for a wide range of dopings and

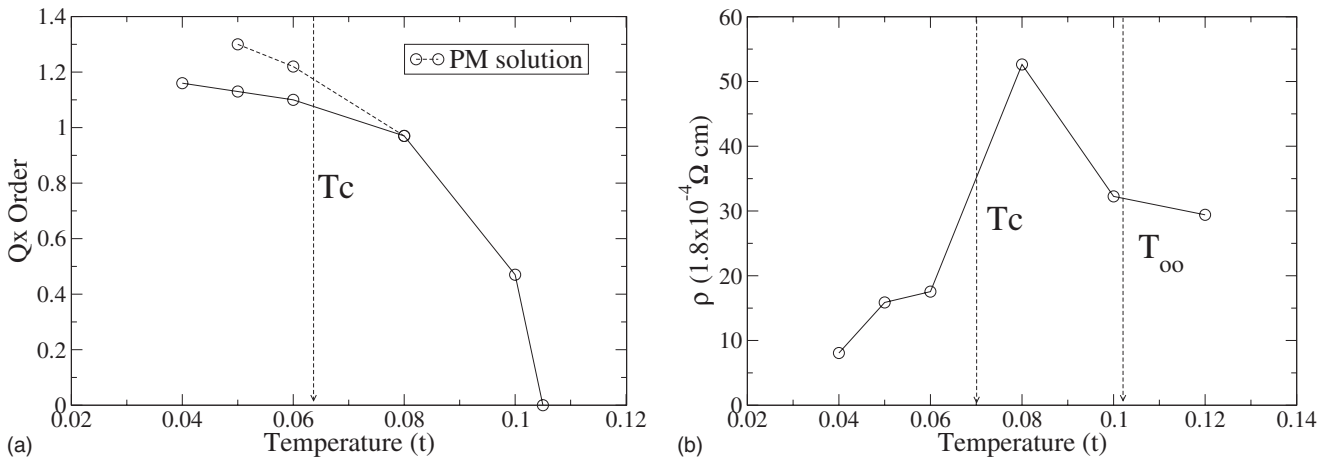

FIG. 11. (a) The amplitude of staggered Q_x order as a function of temperature. The dashed curve is calculated at paramagnetic phase. (b) Resistivity for $x=0.2$ ($N=0.8$) as a function of temperature. The vertical dashed lines indicate the transition temperatures.

TABLE II. The compositions of *A*-site elements, their corresponding Mn-O-Mn angles, and effective hoppings *t*.

A-site	Bond angle	Hopping (ratio)
La_1, ideal	180	0.65 eV (1)
$La_{0.7}Sr_{0.3}$	166	0.58 eV (0.9)
$La_{0.7}Ca_{0.3}$	160	0.53 eV (0.81)
La_1, real	155	0.5 eV (0.78)

temperatures. We believe these agreements to experiments indicate that our model and fittings capture the essential physics of the manganite problem. In this section we give a more detailed discussion on several issues and on inconsistencies with data regarding our results.

B. Role and effect of $GdFeO_3$ rotation

Our results indicate that the local interaction strength is only slightly stronger than the critical value of Mott transition,[20] implying that the system is very sensitive to the hopping *t*. As discussed in Refs. 8 and 26, the hopping is very sensitive to the structure. In particular the manganites form in a distorted version of the ideal perovskite structure. The most important distortion appears to be a $GdFeO_3$-type rotation which buckles the Mn-O-Mn bond. Table II summarizes the relation between the bond angle, the cation composition, and the hopping. For a perovskite material $AMnO_3$, the Mn-O-Mn bond-angle as a function of *A*-site composition is taken from Ref. 26 and the corresponding hoppings were calculated in Ref. 8. From this table we infer that using the same hopping $t=0.5$ eV for $LaMnO_3$ and Ca-doped manganite is reasonable, but is not for the Sr-doped one.

In Ref. 20, we showed that for $t=0.65$ eV $LaMnO_3$ is not a Mott insulator. When using $t=0.6$ eV to simulate $La_{0.7}Sr_{0.3}MnO_3$, we find that: (1) the Curie temperature increases from ~420 K ($t=0.5$ eV) to ~530 K (shown in the dashed curve in Fig. 4) and (2) the high-temperature PO/PM phase becomes almost metallic [$d\rho/dT$ is very flat, and the minimum around $\sigma(\omega=0)$ almost vanishes]. The optical conductivities for $t=0.6$ eV for two temperatures, just above and below T_C, are shown in Fig. 12. Both of our findings [T_C and $\sigma(\omega)$] are consistent with the difference between $La_{0.7}Sr_{0.3}MnO_3$ and $La_{0.7}Ca_{0.3}MnO_3$ reported in Ref. 17. We emphasize, however, that the main message here is that for the given local interaction strength, the system is very sensitive to the bandwidth and any uncertainty in estimating parameters could easily drive the system to either Mott insulating or metallic phases.

C. Orbital ordering

We found that with our standard parameters, the calculated T_{OO} decreases too slowly as a function of doping *x* (see Fig. 4). Fine-tuning parameters (e.g., varying ϵ and U_Q) can correct this problem, but this degree of data fitting is somewhat arbitrary so we do not pursue it here.

However, we point out that using our standard parameters, the orbitally disordered and orbital ordered phases behave very similarly as far as the excitation is concerned. To demonstrate this we show in Fig. 13 the optical conductivities for $x=0.3$ and $T=0.08t$ at both OO and PO phases. One sees that the difference is very limited. Furthermore we found that the Curie temperatures obtained from these two phases are very close (difference <5%). These results suggest that the crucial electronic physics is controlled by local distortions which (because the correlations are strong) are well formed. The important effect caused by the orbital order is actually the uniform Q_z order which introduces an isotropy to the system and whose sign substantially affects the Néel temperature for the undoped case.

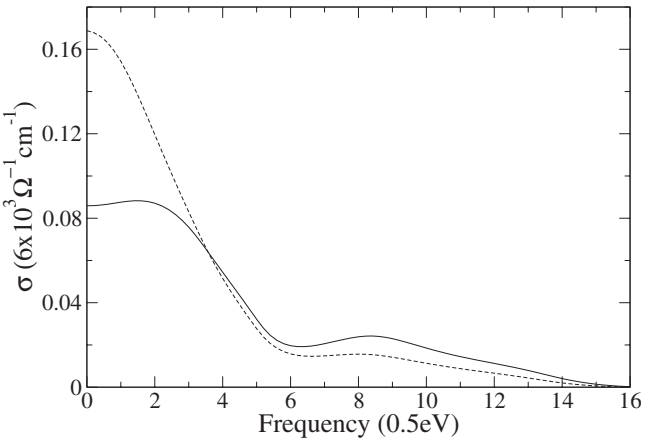

FIG. 12. The optical conductivities calculated for parameters which simulate $La_{0.7}Sr_{0.3}MnO_3$. Solid and dashed curves are computed above and below the Curie temperature. To convert the frequency into physics units (eV), divide the *x* axis by 2.

We also mention here that the effective Mn-Mn hopping being through oxygen *p* orbitals also introduces an intersite orbital coupling[29] which is very similar to the cooperative JT effect and is referred to as the "charge-transfer" mechanism. This can be understood from the superexchange argument where we consider a simple Mn-O-Mn system and compare energies of different orbital configurations by the perturbation expansion of the Mn-O hopping t_{pd}.[30] In the model where the oxygen orbitals are not included, those "virtual

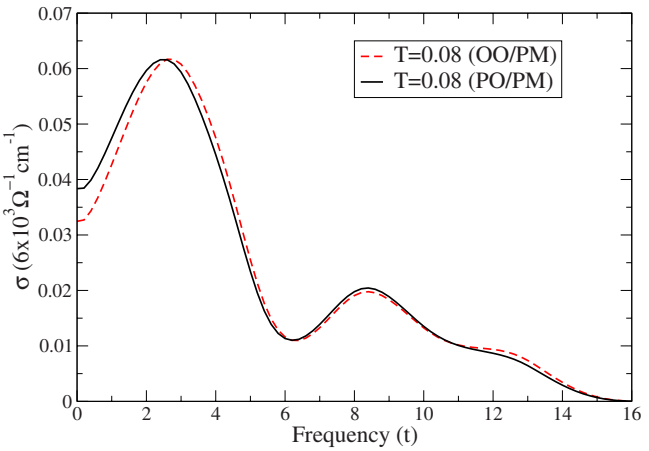

FIG. 13. (Color online) The optical conductivities calculated at $x=0.3$ and $T=0.08t$ for PO (solid) and OO (dashed) phases.

processes" lead to an spin-independent orbital-exchange interaction[29] as

$$H_{\text{o-ex}} = A \sum_{i,\alpha=x,y,z} I_i^\alpha I_{i+\alpha}^\alpha, \tag{19}$$

with $I^z=\tau_z$, $I^x=-\frac{1}{2}\tau_z-\frac{\sqrt{3}}{2}\tau_x$, $I^y=-\frac{1}{2}\tau_z+\frac{\sqrt{3}}{2}\tau_x$, and A as a *positive* coefficient. The simple mean-field approximation to the term produces an external field on site O as

$$\begin{aligned} H_{\text{o-ex}} &= A \sum_{\alpha=x,y,z} I_o^\alpha (\langle I^\alpha \rangle_{+\alpha} + \langle I^\alpha \rangle_{-\alpha}) \\ &= A\left[\tau_z \frac{1}{\sqrt{6}}(2E_z - E_x - E_y) + \tau_x \frac{1}{\sqrt{2}}(-E_x + E_y) \right], \end{aligned} \tag{20}$$

with $E_z=\frac{2}{\sqrt{6}}\Sigma_{\alpha=\pm z}\langle\tau_z\rangle_\alpha$ and $E_{x(y)}=\frac{-1}{\sqrt{6}}\Sigma_{\alpha=\pm x(\pm y)}[\langle\tau_z\rangle_\alpha +(-)\sqrt{3}\langle\tau_x\rangle_\alpha]$, which is of the same form of the cooperative JT effect derived in Appendix B. Therefore in our approximation where the orbital order and structural JT distortions are equivalent, including the charge-transfer mechanism amounts to a reinterpretation of our cooperative JT parameter $\epsilon=2A$ and does not change any results.

D. High-T insulating phase

Using the standard parameters, our calculation obtains an insulating behavior at high-T PO/PM phase for doping ranging from $x=0$ to $x\sim 0.4$. With the semiclassical approximation, the electron-electron interaction is replaced by some classical fields and the impurity problem becomes polaronlike.[7,16] The high-T insulating phase away from zero doping should be therefore interpreted as a phase separation between $N=1$ orbitally fully polarized state and $N=0$ state. Since our estimate indicates[20] that the on-site Coulomb interaction is roughly three times stronger than the electron-lattice interaction, the semiclassical method may overestimate the insulating behavior under single-site DMFT approximation.

The other issue is that compared to the experiments, our calculations overestimate the optical conductivity around zero frequency at high-temperature PO/PM phase. This might be due to short-ranged correlations not included in the single-site DMFT approximation. According to recent cluster DMFT studies of the one-band Hubbard model,[31,32] including the short-range correlation significantly reduces the low-energy density of states. We also observe that in doped CMR systems there is a strong empirical association between insulating behavior ($d\rho/dT<0$ with ρ as dc resistivity and T as temperature) and strong short-ranged Jahn-Teller (polaron glass) order.[33–35] Including spatial correlations beyond the single-site approximation is an important topic for future regard.

E. Missing phases

Our calculation misses two phases. First around $x=0.5$, a charge-ordered (CO) phase occurs, accompanied by one particular orbital and magnetic order called CE phase[1] which requires a very large unit cell (4×4) on the x-y plane. Our in-plane unit cell is not large enough to include this phase. However at $x=0.5$ we do find that the convergence becomes more and more difficult when lowering the temperature (below $T=0.04t$), which may be an indication of CE phase. Second, around $x=0.1-0.2$ we do not get the FM insulating phase at low temperature.

F. Limits of approximation

Now we discuss the limits of our approximation. First we discuss the breathing-mode polaron effect. In the current approximation the breathing-mode coupling is treated in simple mean field and therefore has no effect in the charge-uniform phase. To include the breathing-mode polaron, one has to consider the fluctuation of the breathing-mode distortion by integrating over Q_0 field when computing the impurity model.[16] Since the real time-consuming computation involved in our approach is doing multidimensional integral (see Sec. III C), performing an additional integral is now beyond our computational power. It is possible that the breathing-mode polaron is also crucial for the charge order at $x=0.5$. Since with breathing-mode polarons electrons are already localized but just randomly distributed at high temperature [therefore the system is not charge uniform, but can be treated within single-site DMFT (Ref. 16)], the CO phase is then formed at low temperature to gain more energy from the gap. Without the polaron to localize electrons, it is very hard to get CO phase (usually it requires some nesting in the band structure, which is not the case here).

Finally we point out that the SCA does not treat the quantum physics of the Mott insulator faithfully. To be specific, we take the one-band Hubbard model with strong coupling as an example. With the SCA the metal/insulator transition occurs at $U\sim U_{c1}$ so the effect of the Kondo peak is absent. Further, independent of doping x, the upper and lower Hubbard bands have the same weight with SCA, while in reality, the upper Hubbard band represents adding one electron to the *occupied* site whose weight is ought to be $1-x$. This consideration implies that the SCA works well at half filling and becomes less reliable away from it. This is illustrated in Fig. 14, which shows the spectral functions for $N=1$ (half filling) and $N=0.8$. We see that in both cases the upper and lower bands have the same weight. For our two-band manganite model in the strong-coupling limit, the SCA solution for PO/PM phase results in four bands with weights $1-x$, $1+x$, $1+x$, and $1-x$ (from low energy to high). However the third peak corresponds to adding one electron to the state with same orbital but opposite spin whose weight should be $1-x$. Based on the same argument we conclude that the SCA for two-band model is more reliable without doping than with doping. A more accurate treatment of the doped phase requires an improved, fully quantum impurity solver.

VIII. CONCLUSION

A general model for bulk manganite, including electron-electron, electron-phonon, and phonon-phonon interactions, is formulated and solved by semiclassical approximation. Our calculation is qualitatively good in the sense that it

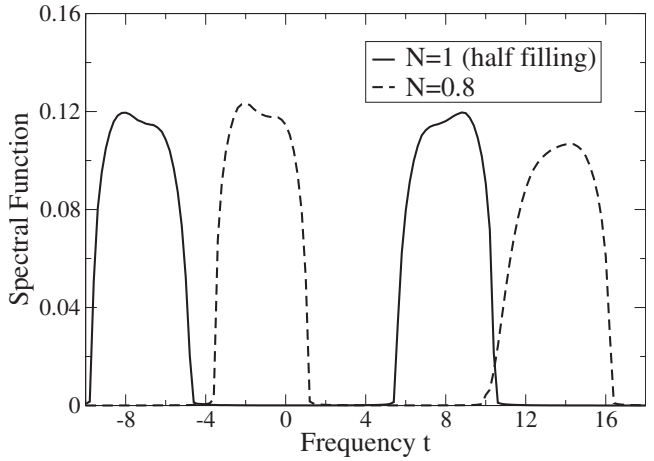

FIG. 14. Spectral function calculated for one-band Hubbard model for bandwidth $6t$ and on-site $U=16t$ at $T=0.1t$. For both half filling (solid) and $N=0.8$ (dashed), the lower and upper bands have the equal weights.

yields the right distribution of phases on the (x,T) plane and produces the correct low-energy excitations as described in Sec. V B. The physical origin of each exhibited phase is identified within our model. For the $LaMnO_3$ below T_{OO}, the exhibited in-plane staggered Q_x order is mostly driven by the cooperative Jahn-Teller (lattice effect) rather than the pure electronic effect, while the uniform $-Q_z$ order is a consequence of the anharmonic term in lattice energy. Our results indicate that the local interaction strength is only slightly stronger than the critical value for Mott transition and the system is consequently very sensitive to mechanisms controlling the effective bandwidth. With this local interaction strength, the orbitally ordered and orbitally disordered phases behave very similarly. As the doping increases, the electrons start to delocalize and after $x>0.3$, the double-exchange mechanism dominates so orbital order vanishes and the system has the FM or metallic ground state.

Discrepancies between our calculation and the observations are also carefully discussed. In particular our calculations overestimate the optical conductivity around zero frequency at high-temperature insulating phase. This inconsistency leads us to conclude that the key physics we are missing in the calculation is the short-ranged correlation. In the future we will include the short-ranged correlation and also adopt a better impurity solver for this problem.

ACKNOWLEDGMENTS

We thank Armin Comanac, Claude Ederer, and Hartmut Monien for many helpful discussions, acknowledge DOE Grant No. DOE-ER46189, and thank the Columbia MRSEC for support.

APPENDIX A: THE VALIDITY OF SEMICLASSICAL APPROXIMATION

In this appendix we examine the validity of the semiclassical approximation by comparing the excitation spectrum computed using the SCA results to the exact eigenstates of the local Hamiltonian. As discussed in Sec. II, we assume that the crystal field (ligand field) is large enough that the t_{2g} levels are in their maximum spin state and that the pair hopping between t_{2g} and e_g orbitals is quenched. In this case the on-site Hamiltonian in the e_g manifold is

$$H_{\rm loc}=\sum_{\sigma,\sigma'}(U-J)n_{1,\sigma}n_{2,\sigma'}+U\sum_{i=1,2}n_{i,\uparrow}n_{i,\downarrow}+J(c^{\dagger}_{1,\uparrow}c^{\dagger}_{1,\downarrow}c_{2,\downarrow}c_{2,\uparrow}+\text{H.c.})-2J\vec{s}_1\cdot\vec{s}_2-2J_H\vec{S}_c\cdot(\vec{s}_1+\vec{s}_2)+\Delta(n_1-n_2). \tag{A1}$$

Here $\vec{s}_i=\Sigma_{\alpha\beta}c^{\dagger}_{i\alpha}\vec{\sigma}_{\alpha\beta}c_{i\beta}$, $\vec{S}_c$ has magnitude of 3/2, and Δ is the crystal-field splitting arising from the long-range Jahn-Teller order. In spherical symmetry $J_H=J$; we assume this henceforth. The eigenstates are characterized by the particle number, total spin, total e_g spin, and the orbital configuration. There are 16 one-electron and 24 two-electron eigenstates, taking the configurations of the core spin into account.

To compare the exact solution of the local Hamiltonian to experiment and the semiclassical calculation, we need the quantity $\Delta E(S)=E(n=2,S)+E(n=0,S=3/2)-2E(n=1,S=2)$ which gives the locations of peaks in the optical conductivity in the atomic limit. Table III lists the eigenstates and the corresponding transition energies.

TABLE III. The two-electron eigenstates and the corresponding transition energies.

State	ΔE	Semiclassical
$^3A_2(5/2)$ (6)	$U-3J/2+2\Delta$	$2U_Q$
$^3A_2(3/2)$ (4)	$U+7J/2+2\Delta$	$2(U_s+J_H)+2U_Q$
$^3A_2(1/2)$ (2)	$U+13J/2+2\Delta$	Not accessible
$^1E^-(3/2)$ (4)	$U+9J/2+2\Delta-\sqrt{4\Delta^2+J^2}$	$2(U_s+J_H)$
$^1A(3/2)$ (4)	$U+9J/2+2\Delta+\sqrt{4\Delta^2+J^2}$	Not accessible
$^1E^+(3/2)$ (4)	$U+7J/2+2\Delta$	$2(U_s+J_H)+2U_Q$

Determining the coupling strength in Eq. (A1) by fitting the optical data[21] is described in detail in Ref. 20. Here we simply quote the results, $U=2.3\pm0.3$ eV and $2\Delta\sim J\sim0.5$ eV. Following the analysis and notations in Ref. 20, there are three optical peaks located at

$$\Delta E_{\rm HS}=U-3J/2+2\Delta,$$

$$\Delta E^{-}_{\rm LS}=U+9J/2+2\Delta-\sqrt{4\Delta^2+J^2},$$

$$\Delta E^{+}_{\rm LS}=U+7J/2+2\Delta. \tag{A2}$$

We now compare this result to the semiclassical calculation. From Fig. 5 we observe three peaks in the optical conductivity: a low-lying peak at energy $2U_Q$ which we identify with $\Delta E_{\rm HS}$, an intermediate peak at energy U_s+J_H which we identify with $\Delta E^{\overline{\rm JT}}_{\rm LS}$, and a higher peak at the sum of these energies. This highest peak represents physically the states $^1E^+(3/2)$ and $^3A_2(3/2)$ where both orbitals are occupied while the total spin (including the core spin) is 3/2. The $^3A(3/2)$ state in the large-Δ limit represents a state where

both electrons occupy energy-disfavored orbital which cannot be reached by a single hopping and has no correspondence in the SCA. It is the defect of the semiclassical approximation that the highest peak is too high in energy. However this defect is not serious because the high-lying states are not important for our analysis.

APPENDIX B: EFFECTIVE POTENTIAL

In this appendix, we describe in detail how we encode the intersite lattice coupling into the single-site impurity problem. The basic logic is the following. First we write down the energy functional for the *lattice* problem in terms of fields labeled by site index ϕ_i which couples to some local quantity ρ_i. Then the *local* partition function is obtained by integrating out all fields except the field at origin site ϕ_0. The long-range order corresponds to some spatial pattern of ρ_i which generates an extra coupling to local field ϕ_0. This extra coupling depends on the long-range order containing information from *other* sites ρ_i, $i \neq o$. We first give a general functional for lattice elastic energy then work out the one-dimensional (1D) case explicitly with a specific lattice model. Finally we derive the formalism used in our calculation.

1. General functional of elastic energy

The goal here is to derive the elastic energy in terms of three even-parity MnO_6 distortion modes. As mentioned in the text, the lattice degree of freedom includes oxygen motion along the Mn-O bond, u_i, and manganese general displacement $\vec{\delta}_i$. Assuming that the spring constant between adjacent Mn-O is $1/K_1$, a general elastic energy is

$$\begin{aligned} E_{\text{lat}} &= \frac{1}{2K_1}\sum_{i,a}[(\delta_i^a - u_i^a)^2 + (\delta_i^a - u_{i-1}^a)^2] + \frac{1}{2}\sum_{\vec{k},ab} E^{ab}(\vec{k})\delta_{\vec{k}}^a \delta_{-\vec{k}}^b \\ &\quad + \frac{1}{2}\sum_{\vec{k},ab} D^{ab}(\vec{k}) u_{\vec{k}}^a u_{-\vec{k}}^b \\ &= \frac{1}{K_1}\sum_{\vec{k},a}[\delta_{\vec{k}}^a \delta_{-\vec{k}}^a + u_{\vec{k}}^a u_{-\vec{k}}^a - (1+e^{+ik_a}) u_{\vec{k}}^a \delta_{-\vec{k}}^a] \\ &\quad + \frac{1}{2}\sum_{\vec{k},ab} E^{ab}(\vec{k})\delta_{\vec{k}}^a \delta_{-\vec{k}}^b + \frac{1}{2}\sum_{\vec{k},ab} D^{ab}(\vec{k}) u_{\vec{k}}^a u_{-\vec{k}}^b, \end{aligned} \tag{B1}$$

where $E^{ab}(\vec{k})$ and $D^{ab}(\vec{k})$ represent general harmonic coupling Mn-Mn and O-O displacements, and a,b sums over x,y,z. To get rid of the Mn motions, we use the saddle-point approximation $\frac{\partial E_{\text{lat}}}{\partial(\delta_{-\vec{k}}^a)} = 0$ which leads to

$$\delta_{\vec{k}}^a = \frac{1}{2K_1}\sum_b [\underline{I} + \underline{E}(\vec{k})/2]_{ab}^{-1}(1+e^{ik_b}) u_{\vec{k}}^b, \tag{B2}$$

and the lattice energy in this approximation is $E_{\text{lat}} = \Sigma_{\vec{k},ab} u_{\vec{k}}^a \tilde{m}^{ab}(\vec{k}) u_{-\vec{k}}^b$, with

$$\tilde{m}^{ab}(\vec{k}) = \frac{\delta^{ab}}{K_1} - \frac{1}{4K_1^2}(1+e^{-ik_a})[\underline{I} + \underline{E}(\vec{k})/2]_{ab}^{-1}(1+e^{ik_b}) + \frac{1}{2}D^{ab}(\vec{k}). \tag{B3}$$

Defining strain variables $v_i^a = u_i^a - u_{i-a}^a$ and $v_{\vec{k}}^a = u_{\vec{k}}^a(1-e^{-ik_a})$, we express E_{lat} in terms of $v_{\vec{k}}^a$, which is

$$E_{\text{lat}} = \sum_{\vec{k},ab} v_{\vec{k}}^a m^{ab}(\vec{k}) v_{-\vec{k}}^b, \tag{B4}$$

where $m^{ab}(\vec{k}) = \frac{1}{1-e^{-ik_a}}\tilde{m}^{ab}(\vec{k})\frac{1}{1-e^{ik_b}}$. The advantage of expressing E_{lat} in strain variables is that they are closer to the even-parity distortion modes defined in Eq. (6). $m^{ab}(\vec{k})$ allows us to estimate the proximity effect for structural order. In particular if we are interested in how $(\pi,\pi,0)$ Q_x order propagates along the z direction, then the quantity to study is $m^{ab}(\pi,\pi,k_z)$. The explicit form of $m^{ab}(\vec{k})$ is model dependent, and here we only consider spring constants between adjacent Mn-O $(1/K_1)$ and Mn-Mn $(1/K_2)$ which are of most importance.

2. One-dimensional Mn-O chain

Now we explicitly work out the local effective potential in the one-dimensional case. The procedure is outlined here. We first adopt the procedure described in Appendix B, Sec. B 1 to express (with saddle-point approximation) the elastic energy in terms of strain variables in real space v_i. Then the effective potential is obtained by integrating out all v_i except the one at origin v_0. For 1D Mn-O chain, we drop the index a,b since there is only one direction and the elastic lattice energy is

$$\begin{aligned} E_{\text{lat}} &= \frac{1}{2K_1}\sum_i [(\delta_i - u_i)^2 + (\delta_i - u_{i-1})^2] + \frac{1}{2K_2}\sum_i (\delta_{i+1} - \delta_i)^2 \\ &= \frac{1}{K_1}\sum_k [u_k u_{-k} + \delta_k \delta_{-k} - u_k \delta_{-k}(1+e^{ik})] \\ &\quad + \frac{2}{K_2}\sum_k \sin^2\left(\frac{k}{2}\right)\delta_k \delta_{-k}. \end{aligned} \tag{B5}$$

For this case, $\frac{E(k)}{2} = \frac{2}{K_2}\sin^2(k/2)$ and $D(\vec{k}) = 0$. The saddle-point approximation $\frac{\partial E_{\text{lat}}}{\partial \delta_{-k}} = 0$ implies

$$\delta_k = \frac{u_k(1+e^{ik})}{2 + 4\bar{K}\sin^2(k/2)}, \tag{B6}$$

where $\bar{K} = K_1/K_2$. The effective energy functional E_{lat} (as a function of u_k only) is therefore

$$\begin{aligned} E_{\text{lat}} &= \frac{2\bar{K}+1}{K_1}\sum_k \frac{\sin^2(k/2)}{1+2\bar{K}\sin^2(k/2)} u_k u_{-k} \\ &= \frac{2\bar{K}+1}{4K_1}\sum_k \frac{1}{1+2\bar{K}\sin^2(k/2)} v_k v_{-k}. \end{aligned} \tag{B7}$$

To see how local strains at different sites couple to one another, we express E_{lat} in the real space v_i,

$$E_{\text{lat}} = \frac{2\bar{K}+1}{4K_1}\sum_k \frac{1}{1+2\bar{K}\sin^2(k/2)} v_k v_{-k}$$
$$= \frac{1}{N}\frac{2\bar{K}+1}{4K_1}\sum_{i,j}\sum_k \frac{e^{ik(r_i-r_j)}}{1+2\bar{K}\sin^2(k/2)} v_i v_j$$
$$= \frac{2\bar{K}+1}{4K_1}\sum_{i,j} f(i-j) v_i v_j, \tag{B8}$$

where

$$f(i-j) = \frac{1}{N}\sum_k \frac{e^{ik(i-j)}}{1+2\bar{K}\sin^2(k/2)}$$
$$= \frac{1}{2\pi}\int_{-\pi}^{\pi} dk \frac{\cos(kn)}{1+2\bar{K}\sin^2(k/2)}$$

($\Sigma_k \to \frac{N}{2\pi}\int_{-\pi}^{\pi} dk$ for lattice constant $a=1$). For this simple model, the integral can be done analytically (the most straightforward way may be changing variable $z=e^{ik}$ and then using the residue theorem). By defining $\alpha = 1 + K_2/K_1$, E_{lat} becomes

$$E_{\text{lat}} = \frac{2\bar{K}+1}{4K_1}\sqrt{\frac{\alpha-1}{\alpha+1}}\sum_{i,j}(\alpha-\sqrt{\alpha^2-1})^{|i-j|} v_i v_j$$
$$= \frac{1}{2K}\sum_{i,j} \epsilon^{|i-j|} v_i v_j, \tag{B9}$$

where $K = 2K_1/\sqrt{2\bar{K}+1}$ and $\epsilon = \alpha - \sqrt{\alpha^2-1} < 1$. Note that the coupling between local strains is exponentially decaying since $\epsilon^n = e^{-a|n|}$ with $a = -\ln \epsilon$.

Including the electron-lattice coupling $\Sigma_i h_i v_i$, the total energy is

$$E = E_{\text{lat}} + E_{\text{e-l}} = \sum_{ij} A_{ij} v_i v_j + \sum_i h_i v_i, \tag{B10}$$

where h_i in this case is the charge density at site i. The effective potential at site 0 is given by integrating out the degrees of freedom of all other sites $v_1, v_2, \ldots, v_N$, i.e.,

$$\int dv_0 e^{-V_{\text{eff}}(v_0)} = \int dv_0 e^{-A_{00}v_0^2} \int dv_1 \cdots dv_N \times \exp\Big[-\sum{}' A_{0i} v_0 v_i - \sum{}' A_{ij} v_i v_j - \sum{}' h_i v_i\Big]$$
$$= \int dv_0 \exp\left[-\left(A_{00} - \frac{1}{4}\sum{}' A_{0i} A_{ij}^{-1} A_{0j}\right) v_0^2 + \frac{1}{2}\sum{}' h_j A_{ij}^{-1} A_{0i} v_0 + \frac{1}{4}\sum{}' h_i A_{ij}^{-1} h_j\right],$$

where Σ' means site 0 is excluded in the summation.

The effective potential is

$$V_{\text{eff}}(v_0) = D v_0^2 - \frac{1}{2}\sum{}' h_j A_{ij}^{-1} A_{0i} v_0 + \text{const}, \tag{B11}$$

where $D = A_{00} - \frac{1}{4}\Sigma' A_{0i} A_{ij}^{-1} A_{0j}$. We see that the charge density at site $h_i (i \neq 0)$ also contribute to the "external" field coupling to v_0.

3. Three-dimensional case

The 1D result can be easily generalized to the three-dimensional (3D) case. For the model we considered, the lattice energy in k space is

$$E_{\text{lat}} = \frac{2\bar{K}+1}{4K_1}\sum_{a=x,y,z}\sum_{k_a} \frac{1}{1+2\bar{K}\sin^2(k_a/2)} v_{k_a} v_{-k_a}. \tag{B12}$$

From this expression, we find that in our simple model there is no proximity effect for $(\pi,\pi,0)$ order of any kind since there is no coupling between different components of $\vec{k}$. We also notice that the energy cost is at its minimum when $k_a = \pi$ (staggered order of any kind). Therefore at integer occupancy the system prefers some staggered long-range order since the staggered order lowers electronic energy.

Assuming that ϵ is small, thus only including the nearest-neighbor coupling, the lattice energy in real space is

$$E_{\text{lat}} = \frac{1}{2K}\sum_{i,a=x,y,z}[(v_i^a)^2 + 2\epsilon v_i^a v_{i+a}^a]. \tag{B13}$$

One can also express E_{lat} in three MnO_6 even-parity modes Q by the following transformation:

$$\begin{pmatrix} Q_{i,0} \\ Q_{i,x} \\ Q_{i,z} \end{pmatrix} = \begin{pmatrix} \frac{1}{\sqrt{3}} & \frac{1}{\sqrt{3}} & \frac{1}{\sqrt{3}} \\ \frac{1}{\sqrt{2}} & -\frac{1}{\sqrt{2}} & 0 \\ -\frac{1}{\sqrt{6}} & -\frac{1}{\sqrt{6}} & \frac{2}{\sqrt{6}} \end{pmatrix} \begin{pmatrix} v_{i,x} \\ v_{i,y} \\ v_{i,z} \end{pmatrix} \equiv U \begin{pmatrix} v_{i,x} \\ v_{i,y} \\ v_{i,z} \end{pmatrix}.$$

However it is more convenient to work in strain field v until we obtain the local effective potential which will be expressed in Q.

The electronic source fields h_i are defined as

$$h_{i,0} = \langle e_{ab} c_{i,a}^\dagger c_{i,b} \rangle,$$
$$h_{i,x} = \langle \tau_{ab}^x c_{i,a}^\dagger c_{i,b} \rangle,$$
$$h_{i,z} = \langle \tau_{ab}^z c_{i,a}^\dagger c_{i,b} \rangle,$$

and the local electron-lattice coupling is

$$E_{\text{JT}} = -h_0 Q_0 - (h_x Q_x + h_z Q_z) = -(v_x H_x + v_y H_y + v_z H_z), \tag{B14}$$

with

$$H_x = \frac{1}{\sqrt{3}} h_0 + \frac{1}{\sqrt{2}} h_x - \frac{1}{\sqrt{6}} h_z,$$

$$H_y = \frac{1}{\sqrt{3}}h_0 - \frac{1}{\sqrt{2}}h_x - \frac{1}{\sqrt{6}}h_z,$$

$$H_z = \frac{1}{\sqrt{3}}h_0 + \frac{2}{\sqrt{6}}h_z. \tag{B15}$$

Following the procedure for one-dimensional case, the effective potential at the origin site is therefore

$$V_{\text{eff}} = D(v_x^2 + v_y^2 + v_z^2) + \frac{1}{2}\vec{E}\cdot\vec{v} \tag{B16}$$

$$= D(Q_0^2 + Q_x^2 + Q_z^2) + \frac{\epsilon}{2}\vec{F}\cdot\vec{Q}, \tag{B17}$$

with $E_{x(y,z)} = \Sigma' H_{j_{x(y,z)},x(y,z)} A^{-1}_{i_{x(y,z)},j_{x(y,z)}} A_{0,i_{x(y,z)}}$ and $\vec{F} = U\vec{E}$. $i_{x(y,z)}$ labels the sites along the $x(y,z)$ axis. We call $\vec{F}$ effective external field. Keeping only the linear term in ϵ, we have

$$D = \frac{1}{2K}(1 - \epsilon^2/4) \sim \frac{1}{2K}, \tag{B18}$$

$$E_x = H_{+\hat{x},x} + H_{-\hat{x},x}$$

$$E_y = H_{+\hat{y},y} + H_{-\hat{y},y}$$

$$E_z = H_{+\hat{z},z} + H_{-\hat{z},z} \tag{B19}$$

and

$$\vec{F} = \left[\frac{1}{\sqrt{3}}(E_x + E_y + E_z), \frac{1}{\sqrt{2}}(E_x - E_y), \frac{1}{\sqrt{6}}(-E_x - E_y + 2E_z)\right]. \tag{B20}$$

[1] J. B. Goodenough, Phys. Rev. **100**, 564 (1955).
[2] E. O. Wollan and W. C. Koehler, Phys. Rev. **100**, 545 (1955).
[3] P. Schiffer, A. P. Ramirez, W. Bao, and S.-W. Cheong, Phys. Rev. Lett. **75**, 3336 (1995).
[4] A. Georges, B. G. Kotliar, W. Krauth, and M. J. Rozenberg, Rev. Mod. Phys. **68**, 13 (1996).
[5] C. Adamo, X. Ke, P. Schiffer, A. Soukiassian, M Warusawithana, L. Maritato, and D. G. Schlom, Appl. Phys. Lett. **92**, 112508 (2008).
[6] A. Bhattacharya, S. J. May, S. G. E. te Velthuis, M. Warusawithana, X. Zhai, A. B. Shah, J.-M. Zuo, M. R. Fitzsimmons, S. D. Bader, and J. N. Eckstein, Phys. Rev. Lett. **100**, 257203 (2008).
[7] S. Okamoto, A. Fuhrmann, A. Comanac, and A. J. Millis, Phys. Rev. B **71**, 235113 (2005).
[8] C. Ederer, C. W. Lin, and A. J. Millis, Phys. Rev. B **76**, 155105 (2007).
[9] L. H. T. R. Hesper and G. A. Sawatzky, Europhys. Lett. **40**, 177 (1997).
[10] A. J. Millis, Phys. Rev. B **53**, 8434 (1996).
[11] K. H. Ahn and A. J. Millis, Phys. Rev. B **58**, 3697 (1998).
[12] J. Kanamori, Jpn. J. Appl. Phys., Suppl. **31**, 14S (1960).
[13] S. Sakai, R. Arita, and H. Aoki, Phys. Rev. B **70**, 172504 (2004).
[14] H. Monien, arXiv:math.NA/0611057 (unpublished).
[15] H. J. Schulz, Phys. Rev. Lett. **65**, 2462 (1990).
[16] A. J. Millis, R. Mueller, and B. I. Shraiman, Phys. Rev. B **54**, 5389 (1996); **54**, 5405 (1996).
[17] M. Quijada, J. Cerne, J. R. Simpson, H. D. Drew, K. H. Ahn, A. J. Millis, R. Shreekala, R. Ramesh, M. Rajeswari, and T. Venkatesan, Phys. Rev. B **58**, 16093 (1998).
[18] L. F. Feiner and A. M. Oles, Phys. Rev. B **59**, 3295 (1999).
[19] J. Rodriguez-Carvajal, M. Hennion, F. Moussa, A. H. Moudden, L. Pinsard, and A. Revcolevschi, Phys. Rev. B **57**, R3189 (1998).
[20] Chungwei Lin and Andrew. J. Millis, arXiv:0808.0733 (unpublished).
[21] N. N. Kovaleva, A. V. Boris, C. Bernhard, A. Kulakov, A. Pimenov, A. M. Balbashov, G. Khaliullin, and B. Keimer, Phys. Rev. Lett. **93**, 147204 (2004).
[22] Y. Okimoto, T. Katsufuji, T. Ishikawa, T. Arima, and Y. Tokura, Phys. Rev. B **55**, 4206 (1997).
[23] K. Tobe, T. Kimura, Y. Okimoto, and Y. Tokura, Phys. Rev. B **64**, 184421 (2001).
[24] K. H. Ahn and A. J. Millis, Phys. Rev. B **61**, 13545 (2000).
[25] K. H. Ahn and A. J. Millis, Phys. Rev. B **64**, 115103 (2001).
[26] *Colossal Magnetoresistive Oxides*, edited by Y. Tokura (Gordon and Breach, New York, 2000).
[27] B. Michaelis and A. J. Millis, Phys. Rev. B **68**, 115111 (2003).
[28] S. J. L. Billinge, Th. Proffen, V. Petkov, J. L. Sarrao, and S. Kycia, Phys. Rev. B **62**, 1203 (2000).
[29] M. V. Mostovoy and D. I. Khomskii, Phys. Rev. Lett. **92**, 167201 (2004).
[30] A. J. Millis, Phys. Rev. B **55**, 6405 (1997).
[31] H. Park, K. Haule, and G. Kotliar, Phys. Rev. Lett. **101**, 186403 (2008).
[32] E. Gull, P. Werner, X. Wang, M. Troyer, and A. J. Millis, Europhys. Lett. **84**, 37009 (2008).
[33] J. W. Lynn, D. N. Argyriou, Y. Ren, Y. Chen, Y. M. Mukovskii, and D. A. Shulyatev, Phys. Rev. B **76**, 014437 (2007).
[34] C. Sen, G. Alvarez, and E. Dagotto, Phys. Rev. Lett. **98**, 127202 (2007).
[35] T. Z. Ward, S. Liang, K. Fuchigami, L. F. Yin, E. Dagotto, E. W. Plummer, and J. Shen, Phys. Rev. Lett. **100**, 247204 (2008).